University of Dundee

University of Dundee

Role of Protein in Fungal Biomineralization of Copper Carbonate Nanoparticles

Liu, Feixue; Shah, Dinesh Singh; Gadd, Geoffrey Michael

Graphical Abstract

Authors

Feixue Liu, Dinesh Singh Shah, Geoffrey Michael Gadd

Correspondence

g.m.gadd@dundee.ac.uk

In Brief

Liu et al. show that triosephosphate isomerase plays an important role in controlling morphology and structure of mycogenic $CuCO_3$ nanoparticles. The results extend understanding of how microbial systems can influence biomineral formation through protein secretion, which is relevant to the synthesis of inorganic protein-based nanomaterials.

Highlights

- Proteins are involved in the formation of mycogenic $CuCO_3$ nanoparticles (CuNPs)

- Triosephosphate isomerase (TPI) exhibited a strong affinity to the CuNPs

- TPI played an important role in controlling nanomaterial morphology and structure

- Proteomics identified key fungal proteins in biomass-free spent culture media

CellPress

Current Biology

Article

Role of Protein in Fungal Biomineralization of Copper Carbonate Nanoparticles

Feixue Liu,[1] Dinesh Singh Shah,[2] and Geoffrey Michael Gadd[1,3,4,*]
[1]Geomicrobiology Group, School of Life Sciences, University of Dundee, Dundee DD1 5EH, Scotland, UK
[2]Division of Cell Signalling and Immunology, School of Life Sciences, University of Dundee, Dundee DD1 5EH, Scotland, UK
[3]State Key Laboratory of Heavy Oil Processing, Beijing Key Laboratory of Oil and Gas Pollution Control, College of Chemical Engineering and Environment, China University of Petroleum, Beijing 102249, China
[4]Lead Contact
*Correspondence: g.m.gadd@dundee.ac.uk
https://doi.org/10.1016/j.cub.2020.10.044

SUMMARY

Biomineralization processes are of key importance in the biogeochemical cycling of metals and other elements by microorganisms, and several studies have highlighted the potential applications of nanoparticle synthesis via biomineralization. The roles played by proteins in the transformation and biologically induced biomineralization of metals by microorganisms is not well understood, despite the interactions of protein and nanoparticles at mineral interfaces attracting much interest in various emerging fields for novel biomaterial synthesis. Here, we have elucidated the association and involvement of fungal proteins in the formation of biogenic copper carbonate nanoparticles (CuNPs) using a carbonate-enriched biomass-free ureolytic fungal culture supernatant. Proteomic analysis was conducted that identified the major proteins present in the culture supernatant. Of the proteins identified, triosephosphate isomerase (TPI) exhibited a strong affinity to the CuNPs, and the impact of purified TPI on CuNP formation was studied in detail. The combined use of scanning electron microscopy (SEM) and confocal laser scanning microscopy (CLSM) confirmed that TPI played an important role in controlling the morphology and structure of the nanomaterials. Fourier transform infrared spectroscopy (FTIR) was applied to examine conformational changes of the proteins to further clarity the interaction mechanisms with CuNPs during biomineralization. Such analyses revealed unfolding of proteins on the mineral surface and an increase in β sheets within the protein structure. These results extend understanding of how microbial systems can influence biomineral formation through protein secretion, the mechanisms involved in formation of complex protein/inorganic systems, and provide useful guidelines for the synthesis of inorganic-protein based nanomaterials.

INTRODUCTION

Many microorganisms, including bacteria, yeasts, and filamentous fungi, are able to produce a variety of nanoscale materials with promising industrial applications.[1–4] Among these microbial groups, fungi are well known for biomineralization of metals, i.e., conversion of free metal ions into insoluble mineral forms, through, e.g., redox transformations and/or metabolite excretion. Such biomineralization can result in the formation of elemental or mineral nanoparticles (NPs) of differing compositions and morphologies.[5,6] For example, *Fusarium oxysporum* can reduce silver ions and generate silver NPs extracellularly.[7] *Neurospora crassa* produces mono- and bimetallic gold/silver NPs intracellularly[8] and cadmium carbonate NPs extracellularly.[9] Metal-containing NP production by biological systems presents some important advantages over traditional chemical syntheses and could help promote clean, non-toxic, and environmentally friendly manufacturing.

The actual mechanisms of formation of many kinds of NPs by microorganisms is still an open question, and the limited knowledge about how to control the properties of final products so far precludes industrial scale bioproduction of NPs. Many researchers have attempted different means of studying the possible mechanisms involved in the biological process and how organic molecules can influence the nucleation and crystal growth of nanoscale biominerals.[1,10,11] Several studies have provided evidence that proteins play an important role in controlling NP formation. An NADH-dependent reductase was found to be responsible for reduction of silver ions and subsequent formation of silver NPs by *Fusarium* oxysporum.[12–14] The reduction of platinum salts to platinum NPs by *F. oxysporum* was achieved in two reduction processes aided by a hydrogenase enzyme.[15] Proteins can act as both reducing and stabilizing agents, and it was reported that gold NPs produced on the surface of *Rhizopus oryzae* biomass remained stable without agglomeration for up to 6 months.[16] Proteins identified from an iterative gene library were shown to influence the morphology of the Au NPs by controlling the gold crystal growth rate.[17]

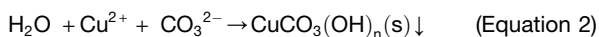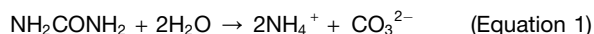Recently, Li et al.[11] and Liu et al.[10] have reported that *Neurospora crassa* was able to mediate production of nanoscale metal carbonate NPs through the reaction of soluble metal ions and carbonate ions that were released from urea hydrolysis. It was

proposed that a change in the conformation of fungal extracellular proteins might provide more NP nucleation sites and promote the crystallization of metal carbonate NPs.[18] In order to clarify the role of extracellular proteins in controlling NP formation, the precipitation of copper carbonate NPs by *N. crassa* was investigated. Cu is an element of interest for electronic and catalytic applications, and the biomineralization of copper-bearing NPs could supply an efficient and affordable method for production of monodispersed NPs. In addition, Cu species show a high affinity to bind to a variety of specific or non-specific proteins. Copper can shift easily between Cu^+ and Cu^{2+} states, with affinities for thiol and thioether groups of cysteine/methionine, and oxygen or imidazole groups of aspartic/glutamic acids or histidine, respectively.[19] In this research, a proteomic study was combined with microscopy and traditional surface chemistry analysis to investigate the association of protein with biogenic CuNPs produced by *N. crassa*. Proteomic analysis provided the first detailed information on protein excretion by *N. crassa*, and the combined use of scanning electron microscopy (SEM) and confocal laser scanning microscopy (CLSM) revealed the spatial relationship of metal ions to proteins at the micrometer scale. The long-term goal of this work was to identify proteins that play an important role in the biomineralization of Cu and other metals, to unravel the interaction mechanisms of proteins and metal NPs, and to inform potential applied protocols for NP surface modification and optimization.

RESULTS AND DISCUSSION

Identification of *N. crassa* Proteins Produced during Growth

In previous work, metal carbonate minerals were found to precipitate by simply mixing soluble metal ion solutions with biomass-free *Neurospora crassa* spent culture media, which was enriched with carbonate ions released from urea hydrolysis by the enzyme amidohydrolase (urease):[9–11]

$$NH_2CONH_2 + 2H_2O \rightarrow 2NH_4^+ + CO_3^{2-} \qquad \text{(Equation 1)}$$

$$H_2O + Cu^{2+} + CO_3^{2-} \rightarrow CuCO_3(OH)_n(s)\downarrow \qquad \text{(Equation 2)}$$

After mixing 20 mM $CuCl_2$ with a biomass-free growth supernatant of *N. crassa*, fine green particles were precipitated, and protein measurements showed that more than 90% of protein was removed from solution by the formation of these copper carbonate minerals. The protein distribution was examined using sodium dodecyl sulfate–polyacrylamide gel electrophoresis (SDS-PAGE), and it was found that the protein pattern of the mineral was strongly consistent with the growth supernatant of *N. crassa*. This indicated that enrichment of the excreted fungal proteins occurred in the produced biominerals (Figure S1). After the biomineralization, there was a dramatic decrease in the protein content of the reactive supernatant, which showed only a few remaining bands for proteins of molecular weights around 15, 20, and 70 kDa. The proteins in the fungal growth supernatant were distributed throughout the entire molecular weight range and representative of the whole proteome. Therefore, the goal of the following proteomic study was to identify the proteins that were potentially involved in the biomineralization of copper carbonate NPs.

Proteomic analysis of the growth supernatant of *N. crassa* was performed in three biological repeats. The results shown in Table 1 are the proteins that were detected in all three tests, with the confidence level >95% and an ionic score (IS) >90 to ensure accurate protein identification.[20] The mass spectrometry results confirmed that 42 proteins were found in the *N. crassa* growth medium, which were related to a variety of metabolic processes, including carbohydrate metabolism, stress responses, and hydrogen peroxide removal. As glucose was used as the sole carbon and energy source for growth, large amounts of proteins involved in glycolysis were detected in the medium. After 12 days of growth, autolysis of aged hyphal structures, resulting in disruption of cell walls, membranes, and organelles, would lead to the release of such proteins originally produced in the cytoplasm, cytosol, and mitochondria to the extracellular environment. Only 12 proteins were detected in the reactive supernatant after copper carbonate NP precipitation (Table S1), and an obvious explanation for such protein subtraction was the association of proteins within the NP structure. It is relevant that many detected proteins require metal cofactors, including Cu, Zn, Mg, Mn, Fe, Co, and others, suggesting that the affinity of these proteins to bind metals could explain their strong association with CuNPs.[21] Another possibility for the binding of proteins and copper NPs is electrostatic attraction. The calculated isoelectric point (IP) of proteins detected in the fungal growth supernatant generally ranged around pH 5–7, lower than the reaction pH = 8.5, which suggested that most of these proteins were negatively charged in the reaction of copper carbonate formation and therefore would tend to combine with positive Cu ions on the biominerals.

Proteins Associated with CuNPs

In order to further study specific proteins and examine their strength of binding to NPs, CuNPs produced from the biomineralization step were washed with increasingly strong solutions of denaturing agents, such as SDS solutions, that facilitate overall desorption of the proteins.[22] The proteins that were still bound to the minerals after washing with the denaturing solutions were precipitated by mixing the NPs with trichloroacetic acid (TCA) solution and loaded onto a SDS-PAGE gel. When the NPs were washed with denaturing solutions, loosely associated proteins were stripped from the NPs, leaving proteins that had relatively higher affinities for the particles still associated with the NPs (Figure 1). ImageJ was used for single protein band quantification, by calculating the relative intensities of the respective bands, with darker bands indicating a higher relative density. Some proteins still remained bound to the minerals even after boiling for 30 min in 10% SDS, indicating a very strong interaction between the proteins and the NPs. The lane of this sample boiled in 10% SDS for 30 min was further studied, and the results for bands A-G are shown in Figure 1B. Band E, with a molecular weight around 25 kDa, showed the highest density compared with other bands, and this band was cut out, and putative proteins were identified by mass spectrometry,[23] the results being shown in the table inserted in Figure 1.

Experiments were run in triplicate, and the results showed that 7 different proteins were detected in all three tests, e.g., enolase, triosephosphate isomerase (TPI), and glucoamylase. Among these, TPI, with a molecular weight of 27,388 Da, showed the

Current Biology
Article

CellPress
OPEN ACCESS

Table 1. Proteins Detected in Biomass-free Spent Culture Medium after Growth of *N. crassa*

Name		Size (kDa)	IP	Cofactor	Function
ENO	enolase	48	5.21	Mg^{2+}	glycolysis
ALF	fructose-bisphosphate aldolase	40	5.42	Zn^{2+}	glycolysis
G6PI	glucose-6-phosphate isomerase	61	6.03		gluconeogenesis, glycolysis
TPI	triosephosphate isomerase	27	5.40		gluconeogenesis, glycolysis
KPYK	pyruvate kinase	58	6.36	Mg^{2+}, K^+	glycolysis
ASD1	putative rhamnogalacturonase	58	8.77		carbohydrate metabolism, cell wall biogenesis/degradation
KATG	catalase-peroxidase	83	5.97		hydrogen peroxide catabolic process
AMYG	glucoamylase	67	5.47		carbohydrate metabolism, polysaccharide degradation
SODC	superoxide dismutase [Cu-Zn]	16	5.74	Cu^{2+}, Zn^{2+}	cell redox homeostasis
HSP88	heat shock protein hsp88	79	5.09		stress response
CAT3	catalase-3	79	5.69	iron (heme axial ligand)	hydrogen peroxide removal
PGK	phosphoglycerate kinase	45	6.17		glycolysis
LAC1	laccase	69	6.70	Cu^{2+}	lignin degradation
CYM1	mitochondrial presequence protease	113	5.84	Zn^{2+}	mitochondrial transit peptides degradation
NDK	nucleoside diphosphate kinase	17	7.82	Mg^{2+}	nucleotide metabolism
SPEE	spermidine synthase	33	5.53		spermidine biosynthesis
CVNH	cyanovirin-N homolog	13	4.73		mannose-binding lectin
GSHR	glutathione reductase	51	5.99		cell redox homeostasis
PDC	pyruvate decarboxylase	63	5.71	metal cation	pyruvate metabolism
CAT1	catalase-1	82	6.21	iron (heme axial ligand)	hydrogen peroxide catabolic process
GRP78	78 kDa glucose-regulated protein homolog	72	4.93		secretory polypeptide translocation
FDH	formate dehydrogenase	41	5.93		formate catabolic process
AMPP1	probable Xaa-Pro aminopeptidase P	76	5.61	Mn^{2+}	removal of a penultimate prolyl residue from the N termini of peptides
GBLP	guanine nucleotide-binding protein subunit beta-like protein	36	6.79		positive regulation of protein phosphorylation
MET3	sulfate adenylyltransferase	65	6.20		hydrogen sulfide biosynthesis
NNRD	ATP-dependent (S)-NAD(P)H-hydrate dehydratase	38	6.41	Mg^{2+}	nicotinamide nucleotide metabolic process
HIS2	histidine biosynthesis trifunctional protein	94	5.52	Zn^{2+}	L-histidine biosynthesis
IPYR	inorganic pyrophosphatase	33	5.28	Mg^{2+}	phosphate-containing compound metabolic process
EIF3B	eukaryotic translation initiation factor 3 subunit B	86	5.00		formation of cytoplasmic translation initiation complex
CARP	vacuolar protease a	43	4.69		protein catabolic process, proteolysis
MASY	malate synthase, glyoxysomal	61	7.27		(S)-malate synthesis from isocitrate
MAP2	methionine aminopeptidase 2	48	5.78	Co^{2+}, Zn^{2+}, Mn^{2+}, Fe^{2+}	protein initiator methionine removal
MTAP	S-methyl-5′-thioadenosine phosphorylase	34	5.58		L-methionine biosynthesis via salvage pathway
APTH1	acyl-protein thioesterase 1	27	5.99		fatty acid metabolic process, protein depalmitoylation
CISY	citrate synthase, mitochondrial	52	6.73		synthesis of isocitrate from oxaloacetate
LYS1	saccharopine dehydrogenase	41	5.27		L-lysine biosynthesis
NTF2	nuclear transport factor 2	14	4.71		nucleocytoplasmic transport
PDX1	probable pyridoxal 5′-phosphate synthase subunit pdx-1	33	5.85		pyridoxal 5¢-phosphate biosynthesis

CellPress
OPEN ACCESS

Current Biology
Article

Table 1. *Continued*

Name		Size (kDa)	IP	Cofactor	Function
GLYC	Serine hydroxymethyltransferase, cytosolic	53	6.93		interconversion of serine and glycine
EIF3L	eukaryotic translation initiation factor 3 subunit L	55	5.09		protein synthesis of a specialized repertoire of mRNAs
CAPZA	F-actin-capping protein subunit alpha	30	5.91		actin cytoskeleton organization
ARGI	arginase	39	5.71	Mn^{2+}	synthesis L-ornithine and urea from L-arginine

Data show proteins detected after 12-day growth of *N. crassa* in AP1 liquid medium, with a confidence level >95% and an ionic score (IS) >90 in three tests to ensure accurate protein identification. The proteins are ranked from a high to low IS. IP refers to the isoelectric point for each protein. See also Table S1.

highest relative amount, with the highest exponentially modified protein abundance index (emPAI), which enables label-free relative quantitation of the protein in a mixture based on protein coverage.[24] Some proteins, e.g., heat shock protein hsp98, were detected in the 25 kDa gel band but were not detected in the full proteome. A possible explanation is that the relative concentrations of such proteins were too low to be detected in the fungal full proteome, but, if they were enriched in the mineral structure, they could then be detected as a result of their increase in relative abundance.

The morphology of the minerals that were washed in 10% SDS for 30 min was examined by SEM (Figures 1C and 1D). Compared with the homogeneous grains and powder-like structure of copper carbonate NPs (mean size ~30 nm) formed in the fungal medium without any treatment, some particle aggregates, with a size around 400–500 nm, were found after washing in 10% SDS. This confirmed a direct and immediate impact of protein removal on the morphology of CuNPs. NPs have a high surface area to volume ratio, and the total free energy of NPs tends to decrease on reducing the interfacial area to make the system stable, which usually results in particle agglomeration. Some proteins can stabilize NPs dispersed in solution by increasing the forces responsible for interparticle interactions between NPs.[25] Therefore, the removal of proteins from the biogenic NPs washed in 10% SDS decreased the strong repulsive forces, resulting in aggregation of the NPs.

Effect of TPI on the Morphology of CuNPs

In order to investigate the mechanism of protein reactions with NPs in a more controllable manner, the effect of a single purified protein on nanomineral formation was tested. TPI, the protein with the highest relative amount, associated with the CuNPs, was cloned and expressed in *Escherichia coli*. TPI is involved in the synthesis of D-glyceraldehyde 3-phosphate from dihydroxyacetone phosphate in the gluconeogenesis pathway, and, although it is not known to be involved in any metal metabolism and has no metallic cofactors, it showed a strong affinity with the CuNPs. The three-dimensional (3D) structure of the TPI protein was derived from homology modeling, via the calculation and simulation of its amino acid sequence based on a homologous protein of known crystal structure, as shown in Figure 2. The strong binding affinity of TPI toward the Cu minerals was confirmed by the SDS-PAGE gel results (Figure S2), as lanes corresponding to purified TPI and the Cu minerals produced in the presence of TPI both showed strong and clear protein bands

of the correct size, whereas protein bands were not detected in the supernatant after mineral precipitation. This showed conclusively that TPI was strongly binding to the minerals, and therefore most of the protein was removed by mineral precipitation from the reaction system.

The potential impact of purified TPI protein on copper carbonate formation was further investigated, and the biogenic minerals produced in the presence of TPI were compared to chemically synthesized Cu carbonate. Chemically synthesized Cu carbonate minerals, used as a control, were obtained by mixing 20 mM $(NH_4)_2CO_3$ and 2 mM/20 mM $CuCl_2$. Two Cu concentrations were used to investigate the effect of different metal concentrations on the formation of metal-bearing NPs. In order to examine the impact of TPI, TPI was added to the chemical reaction mixture to final concentrations of 0.02 and 0.1 mg/mL, the reaction pH being around pH 8.0 to 8.1. Precipitated minerals were collected and examined by SEM and CLSM to reveal the impact of the associated protein on mineral morphology.

After a 24 h reaction period, few crystallization nuclei were found in the mixture of 20 mM $(NH_4)_2CO_3$ and 2 mM $CuCl_2$, as nuclei in the solution were undersaturated (Figure 3A). No obvious crystalline structures were observed in the samples with 0.02 mg/mL TPI, and sample surfaces were covered by a thin layer of dried organic materials (Figure 3B). NPs with an average diameter of ~60 nm were precipitated when the concentration of TPI was increased to 0.1 mg/mL. Nucleation and growth of NPs can be critically affected by the microenvironment of the particle system. The solution chemistry, pH, and temperature and the addition of biological molecules are believed to be crucial factors.[26] The nitrogen atoms of the amide groups in the protein backbone and some amino acid residues can form complexes with Cu^{2+}.[27] It was observed that proteins were tightly bound within the mineral structure (Figure 1C). At early stages of crystal growth, such biomolecules are bound to mineral surfaces, resulting in the blocking of growth sites on the surface of copper carbonate particles after "burst nucleation," resulting in the formation of NPs. In the reaction of 20 mM $(NH_4)_2CO_3$ and 20 mM $CuCl_2$ (Figures 3D–3F), micrometer-scale spherical particle agglomerations made of large numbers of nanocrystals were formed. Compared with the morphology of samples without TPI or with 0.02 g/L TPI (Figures 3D and 3E), the addition of a high concentration of protein (0.1 mg/mL TPI) enabled the formation of more dispersible particles and retarded particle aggregation. The formation of NPs with diameters
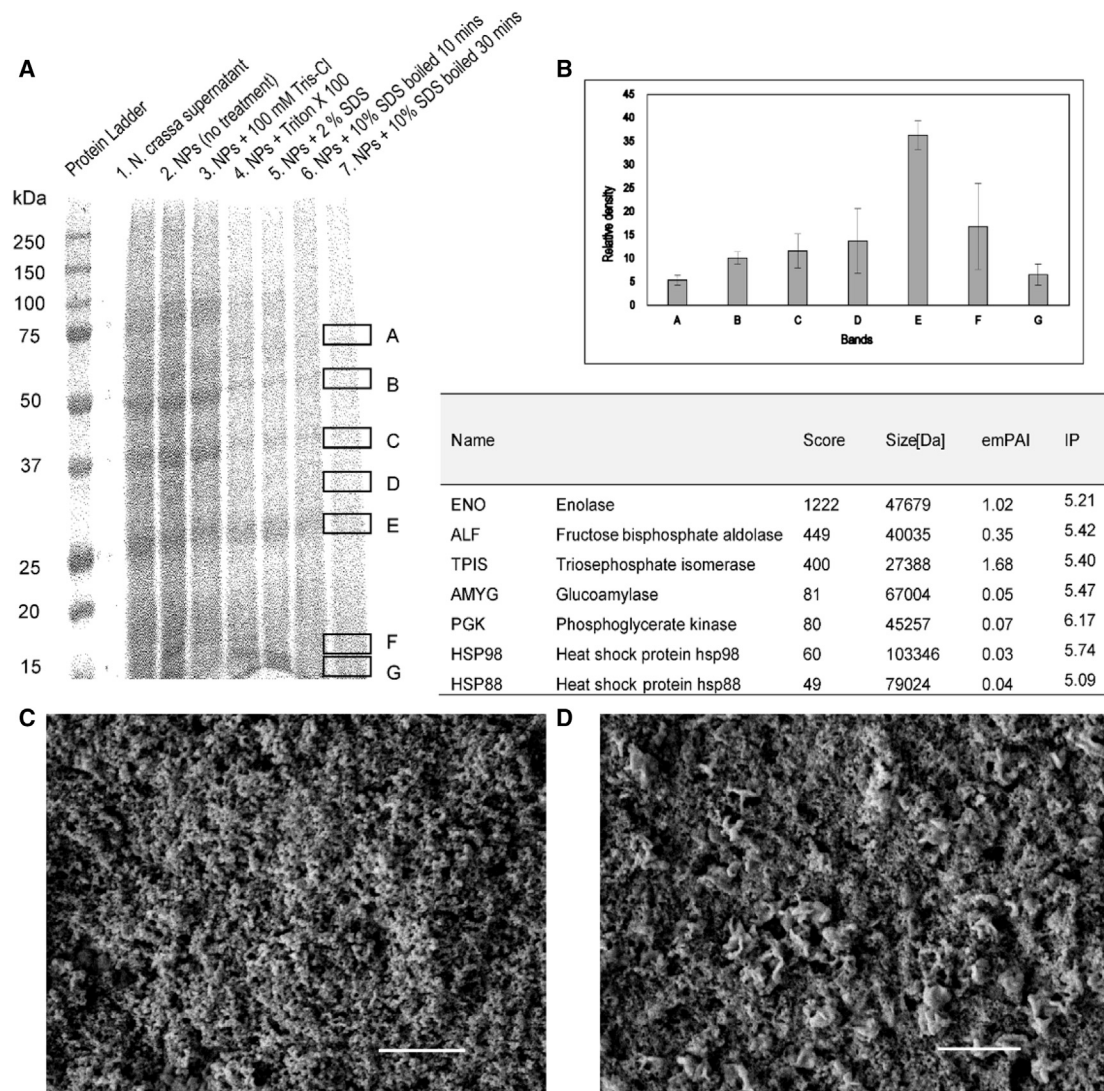
Current Biology
Article

CellPress
OPEN ACCESS

Name		Score	Size[Da]	emPAI	IP
ENO	Enolase	1222	47679	1.02	5.21
ALF	Fructose bisphosphate aldolase	449	40035	0.35	5.42
TPIS	Triosephosphate isomerase	400	27388	1.68	5.40
AMYG	Glucoamylase	81	67004	0.05	5.47
PGK	Phosphoglycerate kinase	80	45257	0.07	6.17
HSP98	Heat shock protein hsp98	60	103346	0.03	5.74
HSP88	Heat shock protein hsp88	49	79024	0.04	5.09

Figure 1. Association of *N. crassa* Proteins with CuNPs

(A) 12% SDS-PAGE of copper carbonate NPs precipitated from *N. crassa* phosphate-free AP1 medium: from left to right shows samples of the protein ladder, (1) *N. crassa* culture medium supernatant, (2) NPs without any pre-treatment, and NPs treated with (3) 100 mM Tris-Cl, (4) Triton X-100, (5) 2% SDS, (6) 10% SDS and boiling for 10 min, and (7) 10% SDS boiling for 30 min. See also Figure S1.

(B) Relative densities of gel bands calculated by ImageJ. The error bars are shown as one standard error.

(C) SEM image of CuNPs produced from *N. crassa* growth supernatant without any pre-treatment.

(D) SEM image of CuNPs produced from *N. crassa* growth supernatant after boiling in 10% SDS for 30 min. The scale bars are 1 μm, and typical images are shown from several separate determinations. The inserted table shows identified proteins binding to CuNPs, with ionic score, size, emPAI (exponentially modified protein abundance index), and IP (isoelectric point) for each protein.

See also Figure S1 and Table S1.

around 100 nm was observed with 2 mM CuCl$_2$ and 0.1 g/L TPI after 14 days (Figure 3I), compared with the inorganic control sample that showed spherical structures with diameters in micrometers (Figure 3G). The NP-protein complexes formed at early reaction stages could supply more nucleation sites for crystallization and further promote the development of the NPs. Continuous attachment of CuNPs to the NP-protein surface can also be the result of strong electrostatic forces.[28] The addition of proteins to excess can therefore inhibit or promote nucleation rate and crystal growth, determine the morphology of the

final product, and may also enhance the stability of NPs, and prevent particle aggregation.[29]

These results therefore show that TPI can play an important role in the biomineralization of nanoscale CuNPs. We used a commercial protein, bovine serum albumin (BSA), and another purified *N. crassa* protein [Mn] superoxide oxidase (SOD), the latter having a similar molecular weight (27,804 Da) as TPI, as positive controls in order to compare the impact of various proteins on the morphology of copper carbonate NPs. As shown in Figure S3, after a 14-day reaction between 2 mM CuCl$_2$, 20 mM
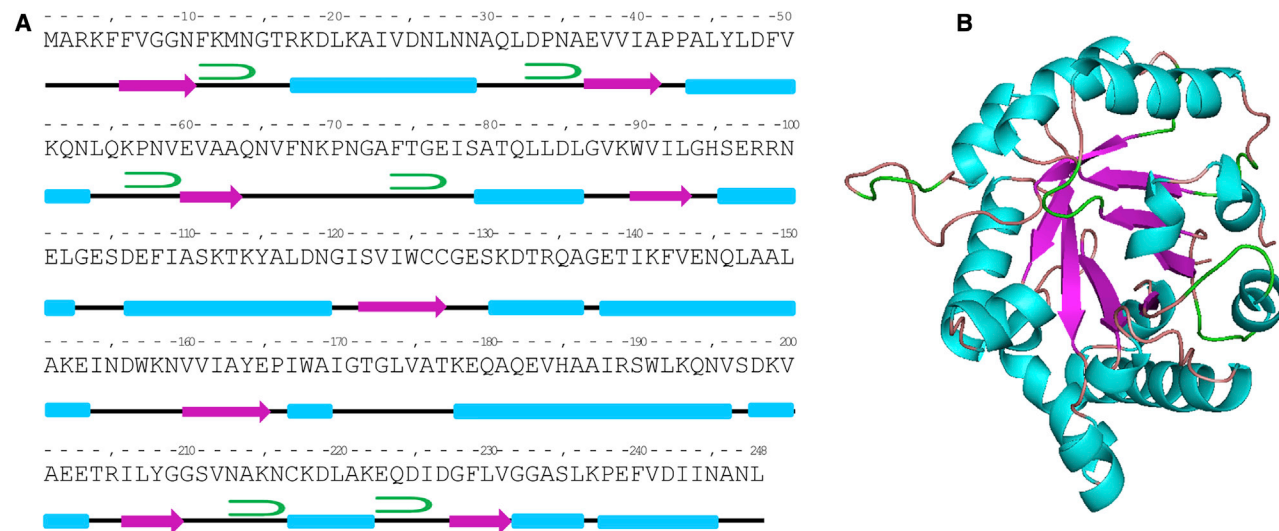
Figure 2. Protein Sequence and Secondary Structure Prediction for *N. crassa* TPI

(A) A secondary structure prediction for *N. crassa* TPI amino acid sequence showing α helices in magenta, β sheets as blue arrows, and β-turns as green hairpins. (B) Protein 3D structural model calculated using SWISS-MODEL workspace (https://swissmodel.expasy.org/). Homology modeling of TPI showed the percentage of α helices in the original TPI protein to be 48.8%, β sheets 15.3%, and β-turns 9.7%.

$(NH_4)_2CO_3$, and 0.1mg/mL protein, the formation of spherical particle agglomerations was extensive, and single NPs were not observed. As mentioned previously, TPI was chosen as a target protein as it showed a strong affinity to combine with the copper carbonate minerals, and, specifically, the CuNPs produced in the presence of TPI were all in the nanoscale range. Products synthesized with other proteins were micro-scale and formed by aggregation. Different protein sizes and structures therefore resulted in the formation of different Cu-protein complexes, which subsequently influenced crystal development and morphologies of the final minerals. However, stable NPs were not produced from the reaction of TPI with Cu, when $[Cu^{2+}]$ was 20 mM. This suggested that the formation of NPs using the fungal growth supernatant may be the combined effect of several proteins, or even with an impact of other biomolecules such as amino acids[30] and polysaccharides,[31] rather than the sole impact of TPI.

In order to investigate the spatial relationships of minerals and proteins, the minerals produced from the reaction of 20 mM $(NH_4)_2CO_3$, 2 mM $CuCl_2$, and 0.1 mg/mL TPI were examined by CLSM. CLSM is able to reveal the distribution of metals and biomacromolecules in biological samples but has been rarely applied in geomicrobiology.[32] Here, we generated 3D images of protein-mineral aggregates by scanning the specimen at 5 μm intervals and stacking those images. The use of Fura 2AM visualized the distribution of Cu and FilmTracer Sypro stained the protein, enabling the visualization of Cu association with protein as well as spatial information. Figure 4 shows the 3D datasets from CLSM illustrating the interaction of proteins (red) and copper (green). The CLSM images showed strong signals for protein covering the mineral surface and inside the mineral clusters, which might indicate multilayer protein adsorption onto the mineral surface (Video S1). Colocalization analysis was applied to assess the amount of colocalization between the

signals for protein and Cu in the images.[33] The Mander's split colocalization coefficient of each channel can reveal the proportion of signal in that channel that colocalizes with the other channel, with zero meaning no colocalization and one meaning perfect colocalization.[34] The Mander's coefficient for the channel of Cu (M_{Cu} = 0.948) was much higher than for the protein channel ($M_{protein}$ = 0.788) and very close to 1, indicating that Cu therefore strongly colocalized with protein in our samples. This also confirms that the proteins have a major role in formation of the Cu minerals. Following initial nucleation of Cu as a NP-protein complex, the mineral precursor can subsequently interact with more proteins, which results in the formation of a matrix of protein and CuNPs.

Fourier-Transform Infrared Spectroscopy Analysis of Conformational Changes in Proteins

Fourier-transform infrared spectroscopy (FTIR) was conducted to further identify the interactions between the copper minerals and proteins and to provide additional information on chemical composition. Minerals produced in the presence of 0.1 g/L TPI were compared with standard malachite ($Cu_2(OH)_2CO_3$) (Figure 5A). Malachite showed characteristic peaks for CO_3^{2-} at around 1,490 and 1,378 (asymmetric stretch), 1,041 (symmetric stretch), and 816 cm^{-1} (bending mode) in the FTIR spectrum.[35] Broad bands were observed at around 3,400 cm^{-1}, which represented the stretching vibration of intermolecular bonded O-H groups. The biominerals precipitated from the 14-day reaction of 20 mM $CuCl_2$ and 0.1 g/L TPI, which showed a similar pattern to the standard, therefore confirmed as malachite. For the sample produced from the reaction of 2 mM $CuCl_2$ and 0.1 g/L TPI, a strong band appeared around 1,600–1,700 cm^{-1}, which is the characteristic amide I band of proteins describing C = O stretching in protein structures. The Amide II peak of protein occurred around 1,452 cm^{-1}, and it is possible that the
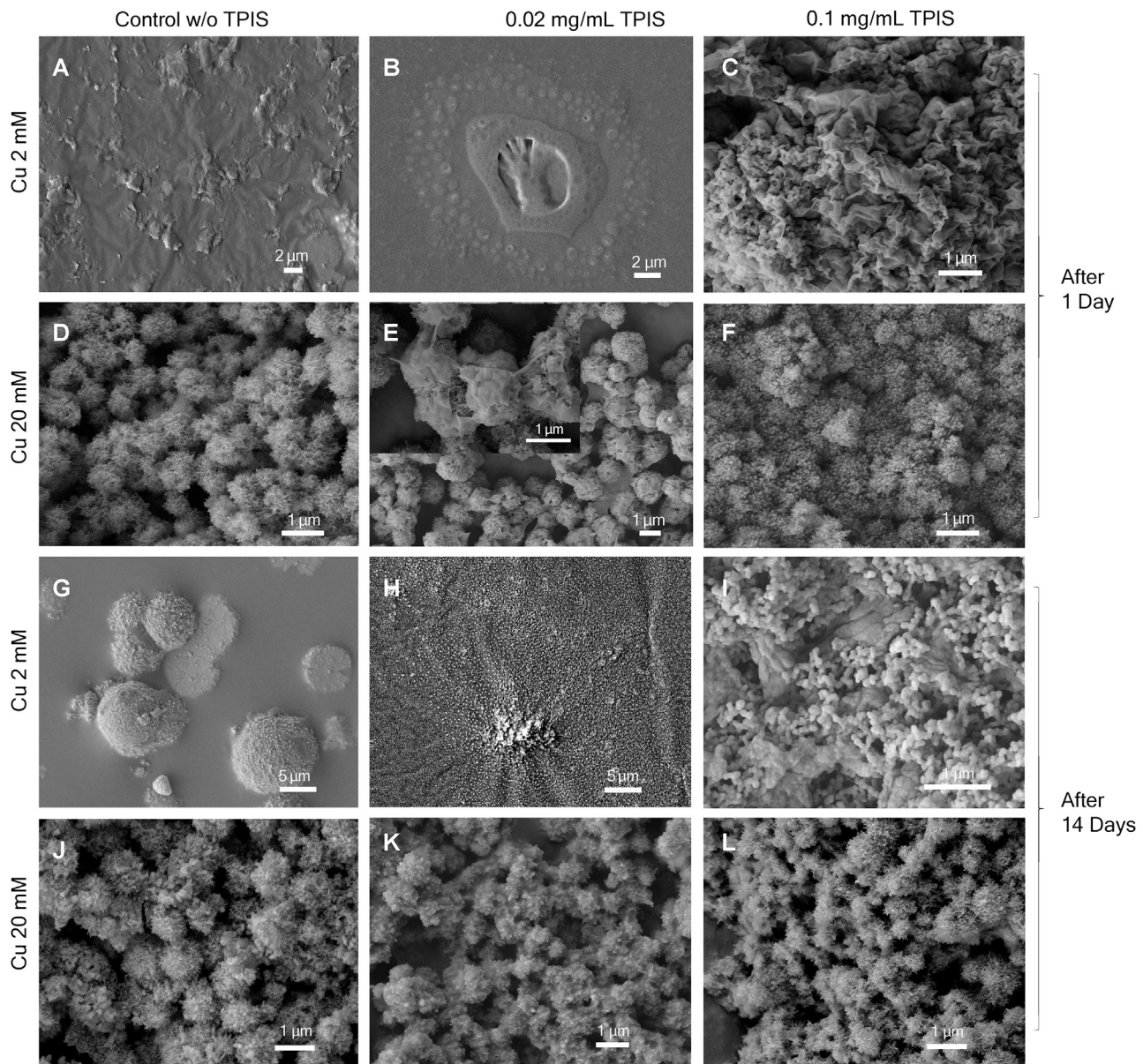
Current Biology
Article

Figure 3. SEM Images of Copper Carbonate Minerals Formed with/without the Addition of TPI

Minerals produced from reactions of (A–C) 20 mM $(NH_4)_2CO_3$ and 2 mM $CuCl_2$ without and with 0.02 and 0.1 mg/mL TPI after a 1-day reaction; (D–F) minerals produced from the reaction of 20 mM $(NH_4)_2CO_3$ and 20 mM $CuCl_2$ without and with 0.02 and 0.1 mg/mL TPI after a 1-day reaction (see also Figure S2); (G–I) minerals produced from the reaction between 20 mM $(NH_4)_2CO_3$ and 2 mM $CuCl_2$ without and with 0.02 and 0.1 mg/mL TPI after a 14-day reaction (see also Figure S3); and (J–L) minerals produced from the reaction between 20 mM $(NH_4)_2CO_3$ and 20 mM $CuCl_2$ without and with 0.02 and 0.1 mg/mL TPI after a 14-day reaction. The scale bars represent 1 μm, and typical images are shown from several separate determinations. See also Figures S2 and S3.

interaction of amide and carbonyl groups through hydrogen bonding shifted the carbonate peak at ~1,490 cm^{-1} to a higher wavenumber (~1,520 cm^{-1}), when compared with standard malachite. The sample that was produced in a protein-enriched environment also showed other protein peaks, such as the Amide III peak (CN stretching, NH bending) at 1,240 cm^{-1}, the Amide IV peak (OCN bending), and additional fluctuations around 3,000–3,400 cm^{-1}, which represent NH stretching.[36] In addition, the occurrence of the peak around 2,960 cm^{-1} is attributable to C-H stretching, which also provides evidence

for the association of organic materials with the mineral structure.[37]

FTIR spectroscopy is a useful tool to determine protein secondary structure, and conformational changes were therefore studied by carrying out deconvolution and curve fitting of the amide I peak (Figures 5B and 5C).[36,38] The Amide I peak can be resolved into peaks attributable to α helices, β sheets, β-turns, and random coils: the percentage content of the different secondary structures in the minerals are shown in Figure 5. Homology modeling of TPI showed that TPI is a helix-
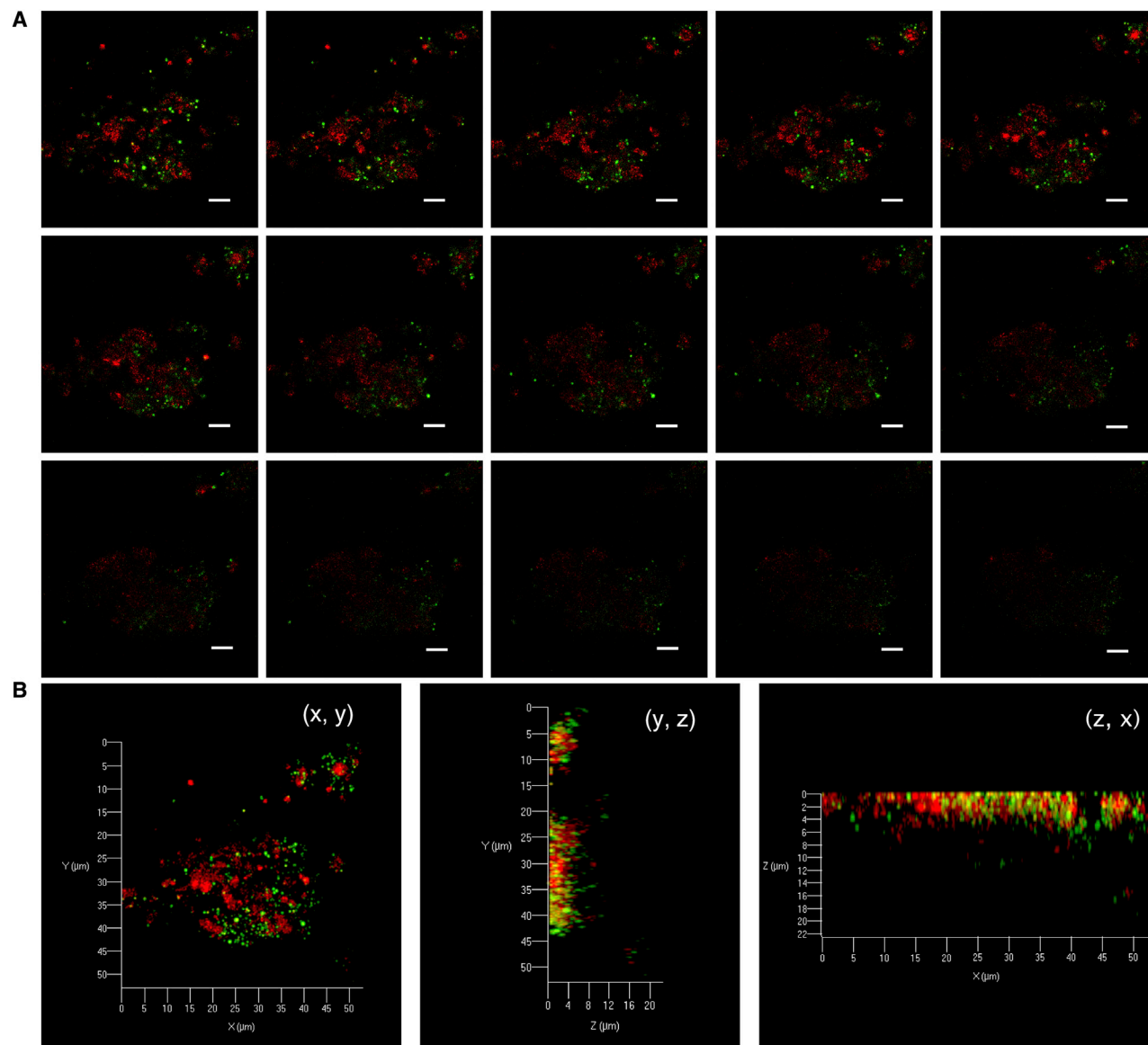
Figure 4. Confocal Microscopy of the Interaction between TPI and Copper Minerals

(A) 15 2D images of the protein-mineral aggregates taken at 5 μm intervals through the sample. The samples were produced by mixture of 20 mM $(NH_4)_2CO_3$ and 2 mM $CuCl_2$ in the presence of 0.1 mg/mL TPI after a 14-day incubation.

(B) 3D data dataset generated from 2D images visualizing the top, side, and front view of the minerals, with proteins shown in red and Cu in green. The scale bars are 5 μm, and typical images are shown from several separate determinations. The colocalization analysis demonstrated that Cu colocalized with protein and that the proteins might supply nucleation sites as a matrix for mineral growth. See also Video S1.

rich protein with a β-barrel structure, with the percentage of α helices in the original TPI protein being 48.8%, β sheets being 15.3%, and β-turns 9.7%. The TPI protein possesses hydrophobic residues (e.g., alanine, valine) orientated into the interior of the barrel, while the polar residues are orientated toward the outside, which makes most β-barrel proteins highly water soluble and hydrophilic. After protein incorporation into the mineral structure, the content of α helices decreased to varying extents: the α helices percentage was 38.4% for minerals synthesized from the reaction of 2 mM $CuCl_2$ and 0.1g/L TPI, but this value decreased for the sample produced with a higher Cu

concentration (20 mM), to 25.7%. A significant increase in β sheet content to 33.7% occurred for the sample produced from reaction of 2mM $CuCl_2$ and 0.1 g/L TPI, which was an increase of 13.4% compared with original TPI. For the sample produced from 20 mM $CuCl_2$ and 0.1 g/L TPI, the β sheet content increased by 8.1% to 23.4% (Figure 5).

Several mineral-protein interactions, including electrostatic attraction, van-der-Waals interactions, hydrogen bonding, and the entropy gain of solvent molecules or counterion release, can induce significant conformational changes in the protein.[39] For a hydrophilic protein with a rich α-helical

Current Biology
Article

CellPress
OPEN ACCESS

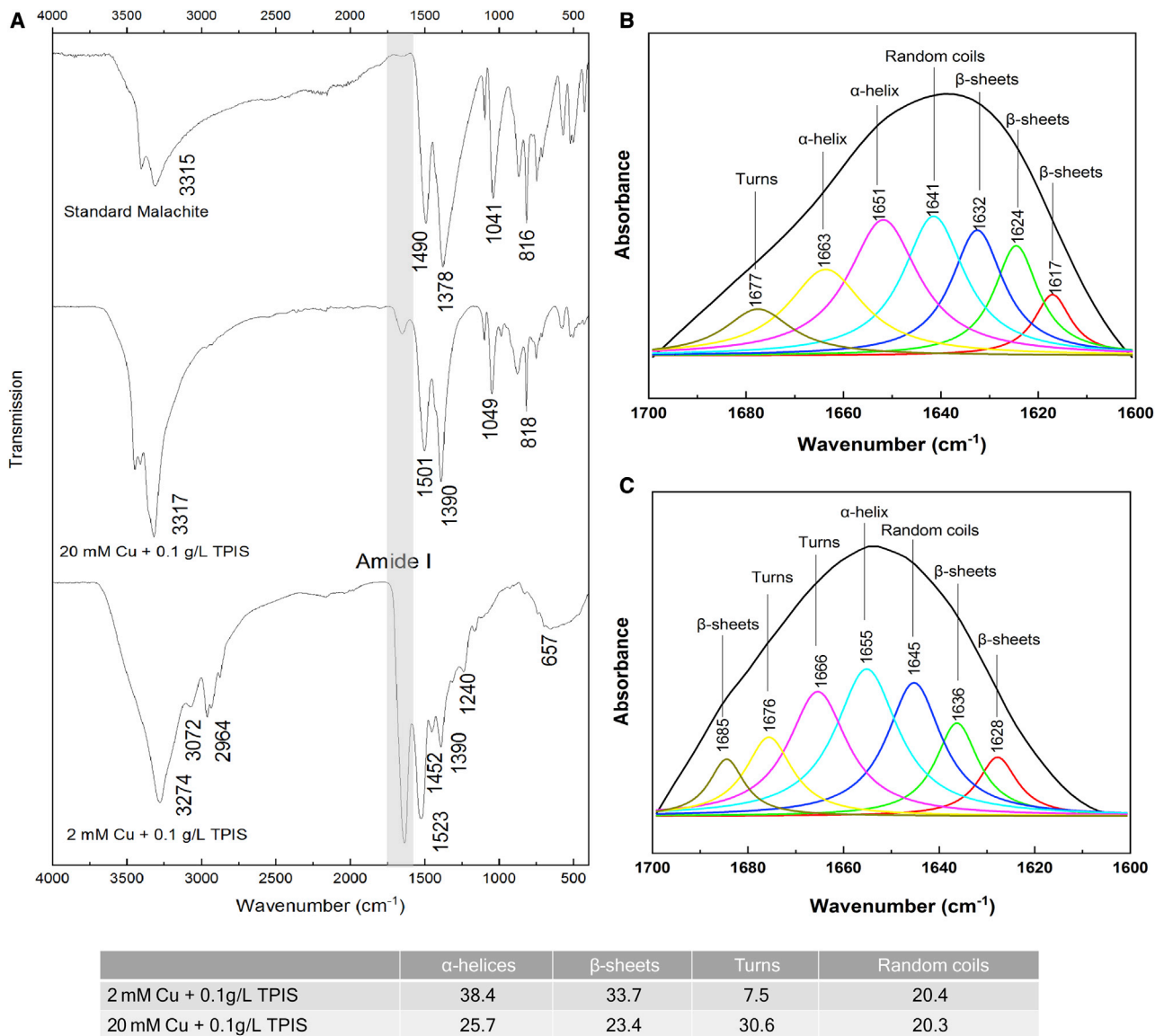|	α-helices	β-sheets	Turns	Random coils
2 mM Cu + 0.1g/L TPIS	38.4	33.7	7.5	20.4
20 mM Cu + 0.1g/L TPIS	25.7	23.4	30.6	20.3

Figure 5. ATR-FTIR Analysis of the Interaction of Proteins with Minerals

(A) FTIR spectrum of standard copper carbonate, and minerals prepared by mixing 2 and 20 mM CuCl$_2$ with 20 mM (NH$_4$)$_2$CO$_3$ in the presence of 0.1 mg/mL TPI after 14 days, respectively.

(B and C) Background subtracted protein amide I band (1,600–1,700 cm^{-1}) curve fitting for secondary structure determination. (B) and (C) were prepared by mixing 20 mM (NH$_4$)$_2$CO$_3$ and 0.1 mg/mL TPI with 2 and 20 mM CuCl$_2$, respectively. The inserted table shows the relative proportion (%) of each secondary structure calculated from peak integration

structure interacting with NPs, the NP surface replaces water molecules on the protein surface. The rearrangement of hydrogen bonds involved in this process results in a decrease in the content of helical structures and other conformational changes.[40] Helices with polar and hydrophilic properties are more prone to attach to NP surfaces,[41] which can explain the strong affinity of TPI with CuNPs. The decrease in the percentage of α helices and an increase in β sheets indicated unfolding of TPI during such association with CuNPs. Similar phenomena have been reported previously for different proteins and various NP surfaces.[42,43] The decrease in α helices was expected to be balanced by an increase in β structures in most cases.[44] The

extra increase in β structures for the sample synthesized from 2 mM CuCl$_2$ and 0.1 g/L TPI can be attributed to a protein-protein reaction, which refers to multiplayer adsorption of the protein molecules or the attachment of more TPI molecules onto the pre-adsorbed TPI. It has been reported that the assembly of protein molecules can result in an increased level of β structures on a mineral surface.[45] The different initial concentrations of Cu^{2+} showed different impacts on the secondary structure of adsorbed TPI for NPs, and the higher [Cu^{2+}] induced more conformational change. This suggests that, when minerals were produced in the presence of a higher metal concentration, the larger surface area of the minerals would supply more sites

for protein adsorption, leading to a higher level of conformational change.

This work has identified the spectrum of proteins produced by *N. crassa* during growth and provided insights into the role of such proteins in the biomineralization of CuNPs. Proteins with a high affinity to bind with CuNPs were screened using proteomic analyses, and further detailed studies on the impact of purified TPI on mineral formation demonstrated the extensive formation of NPs in the presence of TPI. Application of SEM and CLSM revealed the spatial relationship of metal ions to proteins at the micrometer scale. Examination of conformational changes in the protein using FTIR spectroscopy confirmed the association of proteins with the CuNPs and provided further understanding of the NP-protein interactions including conformational changes. As there is no need to maintain living organisms for NP production, a protein-based NP biosynthesis process may offer advantages for potential industrial application. Understanding the interaction mechanisms between proteins and metal NPs may provide protocols for industrial NP surface modification and optimization of production.

STAR★METHODS

Detailed methods are provided in the online version of this paper and include the following:

- KEY RESOURCES TABLE
- RESOURCE AVAILABILITY
  - Lead Contact
  - Materials Availability
  - Data and Code Availability
- EXPERIMENTAL MODEL AND SUBJECT DETAILS
- METHOD DETAILS
  - Biomineralization of copper carbonate nanoparticles (CuNP)
  - Protein identification
  - TPI cloning and expression
  - Impact of TPI on biomineral formation
  - Scanning electron microscopy (SEM)
  - Confocal Laser Scanning Microscopy (CLSM)
  - Attenuated total reflectance–Fourier-transform infrared (ATR-FTIR) spectroscopy
- QUANTIFICATION AND STATISTICAL ANALYSIS

SUPPLEMENTAL INFORMATION

Supplemental Information can be found online at https://doi.org/10.1016/j.cub.2020.10.044.

AUTHOR CONTRIBUTIONS

F.L. and G.M.G. conceived the study and performed the experimental design. F.L. performed biomineral synthesis, proteomic analysis, SEM, and FTIR analysis. D.S.S. performed the CLSM image collection. F.L. and D.S.S. interpreted the obtained data and results. F.L., D.S.S., and G.M.G. wrote the manuscript, and all authors edited and approved the manuscript.

DECLARATION OF INTERESTS

The authors declare no competing interests.

REFERENCES

1. Durán, N., Marcato, P.D., Durán, M., Yadav, A., Gade, A., and Rai, M. (2011). Mechanistic aspects in the biogenic synthesis of extracellular metal nanoparticles by peptides, bacteria, fungi, and plants. Appl. Microbiol. Biotechnol. *90*, 1609–1624.

2. Gadd, G.M. (2010). Metals, minerals and microbes: geomicrobiology and bioremediation. Microbiology (Reading) *156*, 609–643.

3. Sastry, M., Ahmad, A., Khan, M.I., and Kumar, R. (2003). Biosynthesis of metal nanoparticles using fungi and actinomycete. Curr. Sci. *85*, 162–170.

4. Thakkar, K.N., Mhatre, S.S., and Parikh, R.Y. (2010). Biological synthesis of metallic nanoparticles. Nanomedicine (Lond.) *6*, 257–262.

5. Gadd, G.M. (2007). Geomycology: biogeochemical transformations of rocks, minerals, metals and radionuclides by fungi, bioweathering and bioremediation. Mycol. Res. *111*, 3–49.

6. Gadd, G.M., and Raven, J.A. (2010). Geomicrobiology of eukaryotic microorganisms. Geomicrobiol. J. *27*, 491–519.

7. Durán, N., Marcato, P.D., De Souza, G.I.H., Alves, O.L., and Esposito, E. (2007). Antibacterial effect of silver nanoparticles produced by fungal process on textile fabrics and their effluent treatment. J. Biomed. Nanotechnol. *3*, 203–208.

8. Castro-Longoria, E., Vilchis-Nestor, A.R., and Avalos-Borja, M. (2011). Biosynthesis of silver, gold and bimetallic nanoparticles using the filamentous fungus *Neurospora crassa*. Colloids Surf. B Biointerfaces *83*, 42–48.

9. Li, Q., Csetenyi, L., and Gadd, G.M. (2014). Biomineralization of metal carbonates by *Neurospora crassa*. Environ. Sci. Technol. *48*, 14409–14416.

10. Liu, F., Csetenyi, L., and Gadd, G.M. (2019). Amino acid secretion influences the size and composition of copper carbonate nanoparticles synthesized by ureolytic fungi. Appl. Microbiol. Biotechnol. *103*, 7217–7230.

11. Li, Q., and Gadd, G.M. (2017). Biosynthesis of copper carbonate nanoparticles by ureolytic fungi. Appl. Microbiol. Biotechnol. *101*, 7397–7407.

12. Ingle, A., Gade, A., Pierrat, S., Sonnichsen, C., and Rai, M. (2008). Mycosynthesis of silver nanoparticles using the fungus *Fusarium acuminatum* and its activity against some human pathogenic bacteria. Curr. Nanosci. *4*, 141–144.

13. Durán, N., Marcato, P.D., Alves, O.L., Souza, G.I., and Esposito, E. (2005). Mechanistic aspects of biosynthesis of silver nanoparticles by several *Fusarium oxysporum* strains. J. Nanobiotechnology *3*, 8.

14. Ahmad, A., Mukherjee, P., Senapati, S., Mandal, D., Khan, M.I., Kumar, R., and Sastry, M. (2003). Extracellular biosynthesis of silver nanoparticles using the fungus *Fusarium oxysporum*. Colloids Surf. B Biointerfaces *28*, 313–318.

Current Biology
Article

15. Govender, Y., Riddin, T., Gericke, M., and Whiteley, C.G. (2009). Bioreduction of platinum salts into nanoparticles: a mechanistic perspective. Biotechnol. Lett. 31, 95–100.

16. Das, S.K., Das, A.R., and Guha, A.K. (2009). Gold nanoparticles: microbial synthesis and application in water hygiene management. Langmuir 25, 8192–8199.

17. Brown, S., Sarikaya, M., and Johnson, E. (2000). A genetic analysis of crystal growth. J. Mol. Biol. 299, 725–735.

18. Li, Q., Liu, D., Chen, C., Shao, Z., Wang, H., Liu, J., Zhang, Q., and Gadd, G.M. (2019). Experimental and geochemical simulation of nickel carbonate mineral precipitation by carbonate-laden ureolytic fungal culture supernatants. Environ. Sci. Nano 6, 1866–1875.

19. Rubino, J.T., and Franz, K.J. (2012). Coordination chemistry of copper proteins: how nature handles a toxic cargo for essential function. J. Inorg. Biochem. 107, 129–143.

20. Koenig, T., Menze, B.H., Kirchner, M., Monigatti, F., Parker, K.C., Patterson, T., Steen, J.J., Hamprecht, F.A., and Steen, H. (2008). Robust prediction of the MASCOT score for an improved quality assessment in mass spectrometric proteomics. J. Proteome Res. 7, 3708–3717.

21. Aubin-Tam, M.-E., and Hamad-Schifferli, K. (2008). Structure and function of nanoparticle-protein conjugates. Biomed. Mater. 3, 034001.

22. Dobias, J., Suvorova, E.I., and Bernier-Latmani, R. (2011). Role of proteins in controlling selenium nanoparticle size. Nanotechnology 22, 195605.

23. Saptarshi, S.R., Duschl, A., and Lopata, A.L. (2013). Interaction of nanoparticles with proteins: relation to bio-reactivity of the nanoparticle. J. Nanobiotechnology 11, 26.

24. Ishihama, Y., Oda, Y., Tabata, T., Sato, T., Nagasu, T., Rappsilber, J., and Mann, M. (2005). Exponentially modified protein abundance index (emPAI) for estimation of absolute protein amount in proteomics by the number of sequenced peptides per protein. Mol. Cell. Proteomics 4, 1265–1272.

25. Treuel, L., and Nienhaus, G.U. (2012). Toward a molecular understanding of nanoparticle-protein interactions. Biophys. Rev. 4, 137–147.

26. Banfield, J.F., Cervini-Silva, J., and Nealson, K. (2018). Molecular Geomicrobiology Volume 59 (Walter de Gruyter GmbH & Co KG).

27. Sigel, H., and Martin, R.B. (1982). Coordinating properties of the amide bond. Stability and structure of metal ion complexes of peptides and related ligands. Chem. Rev. 82, 385–426.

28. Kim, K.H., Jeong, J.-M., Lee, S.J., Choi, B.G., and Lee, K.G. (2016). Protein-directed assembly of cobalt phosphate hybrid nanoflowers. J. Colloid Interface Sci. 484, 44–50.

29. Jones, F., and Ogden, M.I. (2010). Controlling crystal growth with modifiers. CrystEngComm 12, 1016–1023.

30. Maruyama, T., Fujimoto, Y., and Maekawa, T. (2015). Synthesis of gold nanoparticles using various amino acids. J. Colloid Interface Sci. 447, 254–257.

31. Kang, F., Qu, X., Alvarez, P.J., and Zhu, D. (2017). Extracellular saccharide-mediated reduction of Au^{3+} to gold nanoparticles: new insights for heavy metals biomineralization on microbial surfaces. Environ. Sci. Technol. 51, 2776–2785.

32. Hao, L., Li, J., Kappler, A., and Obst, M. (2013). Mapping of heavy metal ion sorption to cell-extracellular polymeric substance-mineral aggregates by using metal-selective fluorescent probes and confocal laser scanning microscopy. Appl. Environ. Microbiol. 79, 6524–6534.

33. Bolte, S., and Cordelières, F.P. (2006). A guided tour into subcellular colocalization analysis in light microscopy. J. Microsc. 224, 213–232.

34. Dunn, K.W., Kamocka, M.M., and McDonald, J.H. (2011). A practical guide to evaluating colocalization in biological microscopy. Am. J. Physiol. Cell Physiol. 300, C723–C742.

35. Stoilova, D., Koleva, V., and Vassileva, V. (2002). Infrared study of some synthetic phases of malachite $(Cu_2(OH)_2CO_3)$-hydrozincite $(Zn_5(OH)_6(CO_3)_2)$ series. Spectrochim. Acta A Mol. Biomol. Spectrosc. 58, 2051–2059.

36. Kong, J., and Yu, S. (2007). Fourier transform infrared spectroscopic analysis of protein secondary structures. Acta Biochim. Biophys. Sin. (Shanghai) 39, 549–559.

37. Benning, L.G., Phoenix, V., Yee, N., and Tobin, M. (2004). Molecular characterization of cyanobacterial silicification using synchrotron infrared micro-spectroscopy. Geochim. Cosmochim. Acta 68, 729–741.

38. Chittur, K.K. (1998). FTIR/ATR for protein adsorption to biomaterial surfaces. Biomaterials 19, 357–369.

39. Rabe, M., Verdes, D., and Seeger, S. (2011). Understanding protein adsorption phenomena at solid surfaces. Adv. Colloid Interface Sci. 162, 87–106.

40. Mukhopadhyay, A., Basu, S., Singha, S., and Patra, H.K. (2018). Innerview of nanomaterial incited protein conformational changes: insights into designable interaction. Research (Wash D C) 2018, 9712832.

41. Heinz, H., Pramanik, C., Heinz, O., Ding, Y., Mishra, R.K., Marchon, D., Flatt, R.J., Estrela-Lopis, I., Llop, J., and Moya, S. (2017). Nanoparticle decoration with surfactants: molecular interactions, assembly, and applications. Surf. Sci. Rep. 72, 1–58.

42. Schmidt, M.P., and Martínez, C.E. (2016). Kinetic and conformational insights of protein adsorption onto montmorillonite revealed using in situ ATR-FTIR/2D-COS. Langmuir 32, 7719–7729.

43. Givens, B.E., Xu, Z., Fiegel, J., and Grassian, V.H. (2017). Bovine serum albumin adsorption on SiO_2 and TiO_2 nanoparticle surfaces at circumneutral and acidic pH: a tale of two nano-bio surface interactions. J. Colloid Interface Sci. 493, 334–341.

44. Roach, P., Farrar, D., and Perry, C.C. (2006). Surface tailoring for controlled protein adsorption: effect of topography at the nanometer scale and chemistry. J. Am. Chem. Soc. 128, 3939–3945.

45. Chi, E.Y., Krishnan, S., Randolph, T.W., and Carpenter, J.F. (2003). Physical stability of proteins in aqueous solution: mechanism and driving forces in nonnative protein aggregation. Pharm. Res. 20, 1325–1336.

46. Willems, A.P., Gundogdu, M., Kempers, M.J.E., Giltay, J.C., Pfundt, R., Elferink, M., Loza, B.F., Fuijkschot, J., Ferenbach, A.T., van Gassen, K.L.I., et al. (2017). Mutations in N-acetylglucosamine (O-GlcNAc) transferase in patients with X-linked intellectual disability. J. Biol. Chem. 292, 12621–12631.

47. Jiang, L., He, L., and Fountoulakis, M. (2004). Comparison of protein precipitation methods for sample preparation prior to proteomic analysis. J. Chromatogr. A 1023, 317–320.

48. Bradford, M.M. (1976). A rapid and sensitive method for the quantitation of microgram quantities of protein utilizing the principle of protein-dye binding. Anal. Biochem. 72, 248–254.

49. Laemmli, U.K. (1970). Cleavage of structural proteins during the assembly of the head of bacteriophage T4. Nature 227, 680–685.

50. Litvinov, R.I., Faizullin, D.A., Zuev, Y.F., and Weisel, J.W. (2012). The α-helix to β-sheet transition in stretched and compressed hydrated fibrin clots. Biophys. J. 103, 1020–1027.

CellPress
OPEN ACCESS

Current Biology
Article

STAR★METHODS

KEY RESOURCES TABLE

REAGENT or RESOURCE	SOURCE	IDENTIFIER
Bacterial and Virus Strains		
Escherichia coli DH5α competent cells	Invitrogen	Cat#18265017
E. coli BL21(DE3)pLysS competent cells	From Prof Daan van Aalten's lab	[46]
Chemicals, Peptides, and Recombinant Proteins		
Fura 2-AM stain	Abcam	ab120873
FilmTracer SYPRO Biofilm Matrix Stain	Thermal Fisher	F10318
IAA	Abcam	ab146212
DTT	Melford	Cat#3483-12-3
Pierce Trypsin Protease	Thermal Fisher	90057
Critical Commercial Assays		
Coomassie (Bradford) Protein Assay Kit	Thermal Fisher	23200
Deposited Data		
Raw and analyzed datasets	This paper	https://dx.doi.org/10.17632/r2b5g763jj.1
Experimental Models: Organisms/Strains		
Neurospora crassa	FGSC	FGSC: 2489
Oligonucleotides		
TPIS forward oligo: 5′-CGTGGA TCCATGGCTCGCAAGTTCTTC-3′	This paper	N/A
TPIS reverse oligo: 5′-TATGCGGCC GCTTACAGGTTGGCGTTGAT-3′	This paper	N/A
Recombinant DNA		
TPIS cloned in modified version of pGEX6P1 plasmid	This paper	N/A
Software and Algorithms		
ImageJ	NIH	https://imagej.nih.gov/ij/
Excel	Microsoft	https://www.microsoft.com/en-gb/microsoft-365/excel
Origin9.1	OriginLab	https://www.originlab.com/
Mascot Search Engine	Matrix Science	https://www.matrixscience.com/
Swiss-model	SIB	https://swissmodel.expasy.org/
Pymol 2.3.2	Schrödinger	https://pymol.org/2/
Zen	Zeiss	https://www.zeiss.com/microscopy/int/products/microscope-software/zen.html

RESOURCE AVAILABILITY

Lead Contact
Further information and requests for resources should be directed to and will be fulfilled by the Lead Contact, Geoffrey Michael Gadd (g.m.gadd@dundee.ac.uk).

Materials Availability
This study did not generate new unique reagents.

Data and Code Availability
The datasets generated or analyzed during this study are available at Mendeley Data: https://dx.doi.org/10.17632/r2b5g763jj.1.

Current Biology
Article

CellPress
OPEN ACCESS

EXPERIMENTAL MODEL AND SUBJECT DETAILS

The experimental fungus used in this study was *Neurospora crassa* (FGSC: 2489, Fungal Genetics Stock Centre (FGSC), Manhattan, Kansas, USA). After 3d growth on malt extract agar (MEA, Lab M limited, UK) in 90-mm diameter Petri dishes at 25°C in the dark, *N. crassa* was inoculated to a urea-modified AP1 liquid medium (pH = 5.5) consisting of: 2% (w/v) D-glucose (Merck, USA), 40 mM urea (Sigma-Aldrich, USA), 4 mM $K_2HPO_4 \cdot 3H_2O$ (Sigma-Aldrich, USA), 0.8 mM $MgSO_4 \cdot 7H_2O$ (Sigma-Aldrich, USA), 0.2 mM $CaCl_2 \cdot 6H_2O$ (Sigma-Aldrich, USA), 1.7 mM NaCl (Sigma-Aldrich, USA), 9×10^{-3} mM $FeCl_3 \cdot 6H_2O$ (Sigma-Aldrich, USA) and trace metals 0.014 mM $ZnSO_4 \cdot 7H_2O$ (VWR, USA), 0.018 mM $MnSO_4 \cdot 4H_2O$ (Sigma-Aldrich, USA) and 1.6×10^{-3} mM $CuSO_4 \cdot 5H_2O$ (VWR, USA).[9] After 3d growth in complete AP1 medium, fungal biomass was collected and washed twice in sterile Milli-Q water by centrifugation (× 4,000 g, 30 min), and then incubated in sterile phosphate-free AP1 medium for 12 days at 125 rpm, 25°C in the dark.

METHOD DETAILS

Biomineralization of copper carbonate nanoparticles (CuNP)

CuNP were produced following previous protocols.[10] Briefly, *N. crassa* spent culture media was collected by centrifugation (×4,000 g, 30 min) after 12d growth, filtered using a 0.2 μm pore diameter syringe filter, and mixed with $CuCl_2$ solution at a 20 mM final concentration. The samples were placed on a roller shaker (60 rpm) overnight, and precipitated products were collected and washed twice with Milli-Q water by centrifugation (×10,000 g, 30 min).

Protein identification

The original fungal culture medium and reacted supernatant after mineral precipitation were collected, and proteins in solution were precipitated by mixing with a 20% (v/v$_{aq}$) trichloroacetic acid (TCA) (Sigma-Aldrich, USA) overnight at 4°C and then washed twice with acetone.[47] To investigate the association of proteins within the NP structures, pelleted CuNP were washed with (1) 100 mM Tris-Cl (VWR, USA) pH 7.4, (2) 2% Triton X-100 (Sigma-Aldrich, USA), (3) 2% SDS (Melford, UK), (4) 10% SDS and boiling for 10 min and (5) 10% SDS and boiling for 30 min respectively. Some CuNP samples were mixed with the respective denaturing solution, and mixed on a roller shaker at 60 rpm at room temperature for 20 min. Subsequently, all CuNP samples were centrifuged and washed twice with Milli-Q water (10,000 x g, 4°C, 30 min). The carbonate NP dissolved easily in 20% (v/v$_{aq}$) TCA, and the proteins that were bonded to the NP were precipitated and purified using the TCA/acetone method.

The protein samples were quantified using the Bradford assay (Thermal Fisher, USA),[48] and mixed with Laemmli Buffer, boiled for 5 min to denature the protein, and then loaded on a 12% (w/v) SDS-polyacrylamide gel.[49] After running at 200 V for 40 min, the gel was stained with Quick Coomassie Stain (Generon, UK) following the manufacturer's protocol. The relative densities of protein bands were calculated using ImageJ (NIH, https://imagej.nih.gov/ij/). In order to obtain proteomic information, the bands on the gel were cut out and sliced into 1mm pieces, and examined by mass spectroscopy. Briefly, samples were reduced and alkylated with 10 mM dithiothreitol (DTT) (Melford, UK) and 50 mM iodoacetic acid (IAA) (Abcam, UK) respectively to reduce disulfide bonds. Samples were dried and in-gel digested with 12.5 μg/mL trypsin (Thermal Fisher, USA) overnight at 30°C. The peptides were extracted from the gel slices and concentrated using a Speedvac (Eppendorf, Hamburg, Germany). Samples were finally analyzed on an Ultimate 3000 RSLCnano system (Thermo Fisher, USA) coupled to a LTQ OrbiTrap Velos Pro (Thermo Fisher, USA). RAW data files were extracted and converted to mascot generic files (.mgf) and searched against Sprot and the Local peptide database (Mascot Search Engine, Version 2.3.2 https://www.matrixscience.com/) to perform identification.

TPI cloning and expression

Biomass of *N. crassa* grown in AP1 medium for 3d was collected, flash frozen and homogenized in liquid nitrogen by grinding with a mortar and pestle and stored at −80°C until use. Total RNA was extracted using a Monarch Total RNA Miniprep Kit (New England Biolabs, USA) according to the manufacturer's instructions. Single-strand cDNA was synthesized from total RNA using oligo (dT) primer for reverse transcription (qScript cDNA SuperMix, Quantabio, USA). In accordance with the amino acid sequence of TPI from *N. crassa*, two oligonucleotide primers were designed and synthesized (forward oligo: 5′-CGTGGATCCATGGCTCG CAAGTTCTTC-3′; reverse oligo: 5′-TATGCGGCCGCTTACAGGTTGGCGTTGAT-3′). TPI DNA was amplified by the polymerase chain reaction (PCR) using Q5 High-Fidelity DNA Polymerase (New England Biolabs, USA) following the manufacturer's protocol. The final PCR products were isolated from 0.8% agarose/TBE gel and purified using a Monarch DNA Gel Extraction Kit (New England Biolabs, USA). DNA of TPI was cloned as a BamHI-NotI fragment into the pGEX6P1 plasmid (modified version of pGEX which contains a His$_6$ tag instead of GST).[46] The recombinant plasmid was transformed into competent *Escherichia coli DH5α* cells (Invitrogen, Thermo Fisher Scientific, USA) and grown in Luria-Bertani (LB) broth with 100 μg/mL ampicillin overnight. The correct cloning was confirmed by sequencing analysis.

TPI was expressed in *E. coli BL21(DE3)pLysS*[46] by inoculating 1 L of LB medium with 10 mL of an overnight culture grown in the presence of 100 μg/mL ampicillin and allowing it to grow at 37°C until the OD_{600} reached 0.6. The culture was induced with 250 μM isopropyl β-D-1-thiogalactopyranoside (IPTG) (Sigma-Aldrich, USA) and incubated at 18°C, 160 rpm at dark for 20 h. Cells were harvested by centrifugation (3,000 x g, 4°C, 30 min) and the pellet resuspended in lysis buffer (25 mM Tris-Cl pH 7.5, 150 mM NaCl, 0.5 mM TCEP (tris(2-carboxyethyl)phosphine), 0.1 g/L DNase I, 1g/L lysozyme, 1 vial/50 mL protease inhibitor cocktail) and lysed

P **CellPress**
OPEN ACCESS

using a French press. The lysate was centrifuged (20,000 x g, 4°C, 1 h) and the supernatant filtered through 0.45 μm pore size cellulose acetate filters and incubated with Ni-NTA resin (GE Healthcare, USA) for 2 h at 4°C on a rotating shaker (60 rpm). The Ni beads were thoroughly washed using washing buffer (25 mM Tris-Cl pH 7.5, 150 mM NaCl, 0.5 mM TCEP, 30 mM Imidazole pH = 8), and His-tag fusion proteins were eluted using eluent buffer (25 mM Tris-Cl pH 7.5, 150 mM NaCl, 0.5 mM TCEP, 100 mM Imidazole pH = 8). The protein samples were incubated with PreScission protease at 4°C overnight to cleave the His-tag, followed by concentration using a Sartorius Vivaspin ultrafiltration concentrator 10,000 MWCO (Sartorius, Germany) and passing through a HiLoad 26/600 Superdex 75 pg (GE Healthcare, USA) pre-equilibrated with base buffer (25 mM Tris-Cl pH 7.5, 150 mM NaCl, 0.5 mM TCEP). The peak fractions were concentrated to 10 mg/mL and stored at −80°C until use. The protein 3D structure model was calculated in the SWISS-MODEL workspace (https://swissmodel.expasy.org/) based on homology modeling.

Impact of TPI on biomineral formation

Chemically synthesized copper carbonate was used as a control and obtained by mixing 20 mM $(NH_4)_2CO_3$ and 2mM / 20 mM $CuCl_2$ and collecting and washing the precipitate. In order to identify the impact of TPI on biomineralization, TPI was added into the chemical reaction mixture to final concentrations of 0.02 and 0.1mg/mL. The samples were mixed on a roller shaker (60 rpm), and collected by centrifugation (x10,000 g, 30 min) after 1d and 14d reaction times. The precipitated samples were examined by SEM and CLSM to investigate the influence of TPI on their structure and morphology.

Scanning electron microscopy (SEM)

After washing in Milli-Q water twice, a drop of sample suspension was mounted on carbon adhesive tape on aluminum electron microscopy stubs. Samples were air-dried at room temperature overnight in a desiccator, followed by coating with 7 nm gold and platinum using a Cressington 208HR sputter coater (Ted Pella, Redding, CA, USA). SEM images were obtained by using a field emission scanning electron microscope (FESEM) (Jeol JSM7400F) at 5 kV.

Confocal Laser Scanning Microscopy (CLSM)

Biominerals generated during a 14d reaction where 2 mM $CuCl_2$, 20 mM $(NH_4)_2CO_3$ and 0.1 mg/mL TPI were combined were examined by CLSM. Prior to staining, the sample was washed twice and suspended in Milli-Q water. Copper was stained for 30 min at room temperature using 70 μM Fura-2AM (Abcam, UK) in the dark. Fura-2AM stained samples were pelleted and subsequently resuspended in the protein stain FilmTracer Sypro (Thermal Fisher, USA) at room temperature for 20 min in the dark. The protein and copper stained samples were washed twice and resuspended using Milli-Q water. Approximately 3 μL of resuspended samples were encased between a glass slide and a coverslip and sealed using nail varnish. Protein-mineral aggregates were imaged in real time using a Zeiss 710 confocal microscope with a 60x oil-immersion objective at room temperature with excitation (nm) /emission (nm) set at 380/510 for Fura-2AM and 450/610 for FilmTracer Sypro. Zen software was used to process images and to generate 3-dimensional (3D) images (https://www.zeiss.com/microscopy/int/products/microscope-software/zen.html) whereby multiple (up to 20) 2D images taken at 5 μm intervals were combined. Colocalization analysis was applied to quantify colocalization between the signals for protein and Cu in the images by using ImageJ.

Attenuated total reflectance–Fourier-transform infrared (ATR-FTIR) spectroscopy

ATR-FTIR spectra of samples in the form of powders were obtained using a Bruker Vertex 70 FTIR spectrometer (Billerica, Massachusetts, USA). All spectra were measured over the wavelength range from 400 to 4000 cm^{-1}, with a 4 cm^{-1} spectral resolution. Second-derivative spectral analysis was applied to the amide I peak at 1600-1700cm^{-1} after background subtraction, in order to locate the position of the overlapping components of the band. The amide I band was then fitted to a Gaussian curve by Origin 9.1 (https://www.originlab.com/), and the proportion of each component was calculated as the fractional area of the corresponding peak divided by the sum of the area of the amide I band.[50]

QUANTIFICATION AND STATISTICAL ANALYSIS

The density of protein bands was calculated by ImageJ from triplicate tests, and the error bars are shown as one standard error. The typical SEM and CLSM images and spectra are shown from several separate determinations.